Pump Frequency Resonances for Light-Induced Incipient Superconductivity in $YBa_2Cu_3O_{6.5}$

B. Liu[1], M. Först[1], M. Fechner[1], D. Nicoletti[1], J. Porras[3], B. Keimer[3], A. Cavalleri[1,2]

[1]*Max Planck Institute for the Structure and Dynamics of Matter, 22761 Hamburg, Germany.*
[2]*Department of Physics, University of Oxford, Clarendon Laboratory, Oxford OX1 3PU, UK*
[3]*Max Planck Institute for Solid State Research, 70569 Stuttgart, Germany.*

Supplemental Material

S1. Experimental setup

S2. Data acquisition and evaluation

S3. Equilibrium optical properties

S4. Uncertainties in the determination of the transient optical properties

S5. Fitting models

S6. Extended data sets

S7. Pump electric field dependence

S8. Transient response below T_C

S9. Pump-induced heating

S10. Ab-initio calculations of the structural dynamics

References

S1. Experimental setup

The optical setup used to photoexcite $YBa_2Cu_3O_{6.5}$ with tunable narrowband pump pulses and to probe its low-frequency THz response is sketched in Figure S1. It was fed by a 1-kHz repetition rate Ti:sapphire regenerative amplifier, delivering 7-mJ, 80-fs pulses at 800 nm wavelength.

We used 90% of the pulse energy to generate the excitation pulses. To this end, we pumped two parallel home-built optical parametric amplifiers (OPA), which were seeded with the same white light to produce carrier-envelope-phase (CEP) stable THz pump pulses in a subsequent difference frequency generation (DFG) process [1,2]. The two OPA signal outputs of ~120 fs duration were directly sent to a 1-mm thick GaSe crystal to generate the broadband pump pulses at 19.2 THz with relative bandwidth $\Delta\nu/\nu \sim 20\%$. For the generation of narrowband pulses with relative bandwidth $\Delta\nu/\nu < 10\%$, the two signal outputs were linearly chirped to a pulse duration of ~600 fs before the DFG process in either a 0.5 mm thick DSTMS organic crystal [3] or in the same 1-mm GaSe crystal used for the broadband pulses. The pulse energies achieved were always at the few-μJ level. The maximum peak electric fields of the focused beams at the sample surface were 2.9 and 2.7 MV/cm for 4.2 and 10 THz, respectively, and about 3.1 MV/cm for both 16.4 and 19.2 THz pulses. They could be attenuated by inserting a pair of free-standing wire grid polarizers.

Excitation pulses with frequencies above the phonon resonances and up to the near-infrared and visible light regime were either generated by difference-frequency mixing the two OPA outputs in the GaSe crystal, or were taken directly as the output of one of the

OPAs, as the fundamental 800 nm pulses from the Ti:sapphire amplifier, or as their second harmonic generated via type-I phase matching in a BBO crystal.

Single-cycle THz probe pulses with spectral components between 10 and 80 cm^{-1} were generated via optical rectification of 500-μJ pulses at the fundamental 800 nm wavelength in a 500-μm thick ZnTe crystal. The THz electric field of the probe pulses reflected from the sample surface was detected via electro-optic sampling in a 500-μm thick optically contacted ZnTe crystal.

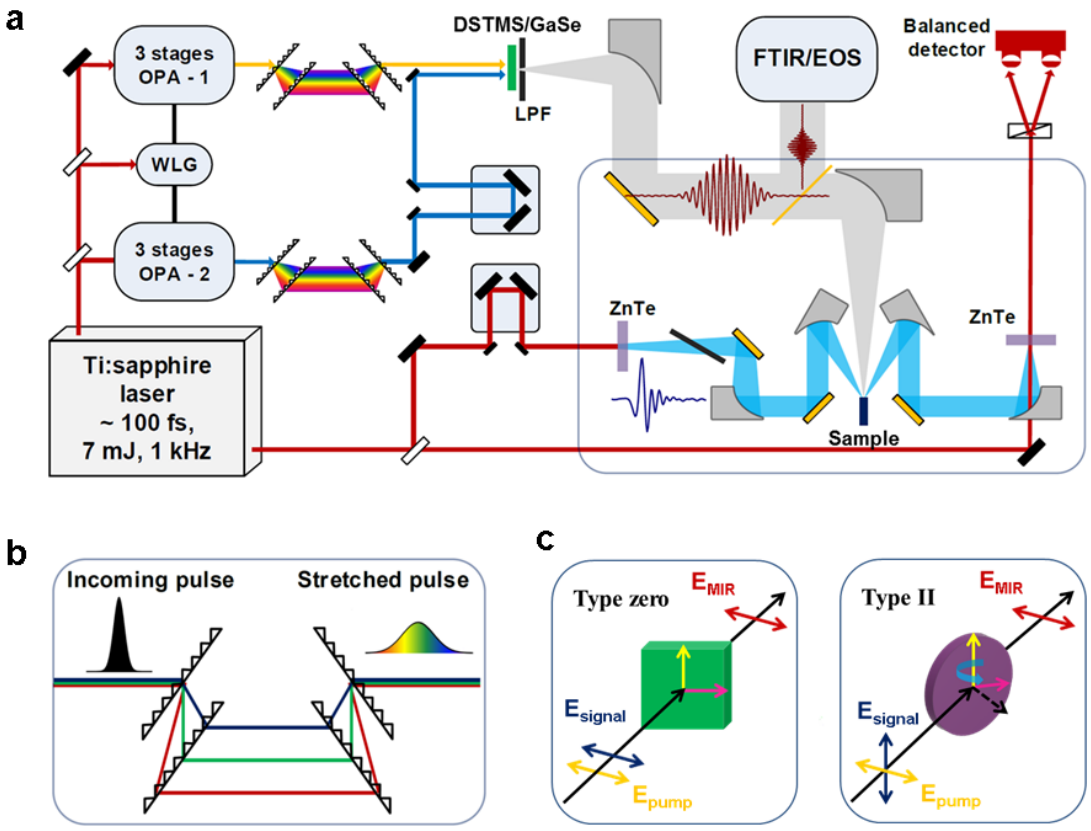

Figure S1. a. Narrowband pump / THz probe setup. OPA, optical parametric amplifier. WLG, white light generation. LPF, long-pass filter. Two near-infrared signal outputs from two parallel OPAs were linearly chirped and sent to a nonlinear crystal (DSTMS/GaSe) for difference frequency generation (DFG). The generated pump pulses were separated from the near-infrared inputs and characterized by either Fourier-transform infrared spectroscopy (FTIR) or electro-optic sampling (EOS). These pump pulses were set to be polarized along the *c* axis of $YBa_2Cu_3O_{6.5}$, with their frequency tuned to be resonant with different phonon modes. The transient optical properties were measured by detecting the THz electric field generated from a ZnTe crystal via optical rectification and reflected from the sample surface, as a function of pump-probe time delay. **b.** Pulse stretcher consisting of four transmission gratings. **c.** Phase-matching condition and DFG process in DSTMS (left) and GaSe (right) crystals.

The experiments were performed on the *ac* surface of a $YBa_2Cu_3O_{6.5}$ single crystal. Pump and probe beams were always polarized along the crystallographic *c* axis. The crystal dimension along this axis (~300 μm) was smaller than the spot size of the pump beam (~400 μm), thus ensuring to probe a homogeneously excited region, independent on the probe spot dimension. A sharp superconducting transition at T_C = 52 K was determined by dc magnetization measurements [4].

S2. Data acquisition and evaluation

Time-domain THz spectroscopy was used to characterize the transient response of $YBa_2Cu_3O_{6.5}$ induced by optical driving. The spectral response at each time delay after excitation was obtained by keeping fixed the delay τ between the pump pulse and the electro-optic sampling gate pulse, and scanning the single-cycle THz probe pulse with internal delay *t* across.

The stationary probe electric field $E_R(t)$ and the differential electric field $\Delta E_R(t,\tau)$ reflected from the sample were recorded simultaneously by feeding the electro-optic sampling signal into two lock-in amplifiers and mechanically chopping the pump and probe beams at different frequencies of ~357 and 500 Hz, respectively. The differential signal $\Delta E_R(t,\tau)$ was sampled at the ~143 Hz difference frequency of the inner and outer wheels of the same optical chopper. This approach minimized the cross-talk between the two detected signals whilst reducing the noise level of the measurements.

The electric field $E_R(t)$ and the differential field $\Delta E_R(t,\tau)$ were independently Fourier transformed to obtain the complex-valued, frequency-dependent $\tilde{E}_R(\omega)$ and $\Delta\tilde{E}_R(\omega,\tau)$. The photo-excited complex reflection coefficient $\tilde{r}(\omega,\tau)$ was determined by [5,6]

$$\frac{\Delta\tilde{E}_R(\omega,\tau)}{\tilde{E}_R(\omega)} = \frac{\tilde{\mathrm{r}}(\omega,\tau) - \tilde{\mathrm{r}}_0(\omega)}{\tilde{\mathrm{r}}_0(\omega)},$$

where $\tilde{\mathrm{r}}_0(\omega)$ is the stationary reflection coefficient known from the equilibrium optical response (see Section S3).

The penetration depth of the excitation pulses was typically smaller than that of the low-frequency THz probe pulses, implying that we were not probing a homogeneously excited sample volume. This mismatch was considered in the data analysis. At each frequency, the penetration depths were calculated by $d(\omega) = \frac{c}{2\omega \cdot \mathrm{Im}[\tilde{n}_0(\omega)]}$ (here $\tilde{n}_0(\omega)$ is the stationary complex refractive index), yielding values of ~5–15 μm for the THz probe and in the range of ~0.1-5 μm for the pump pulses (see also Section S3).

An accurate estimate of the photo-induced optical response functions was then achieved by treating the sample as a layered system, in which only a thin layer below the sample surface is homogeneously excited while the bulk layer below remains unperturbed. The complex reflection coefficient is then expressed as

$$\tilde{\mathrm{r}}(\omega,\tau) = \frac{\tilde{\mathrm{r}}_A(\omega,\tau) + \tilde{\mathrm{r}}_B(\omega)e^{2i\delta(\omega,\tau)}}{1 + \tilde{\mathrm{r}}_A(\omega,\tau)\tilde{\mathrm{r}}_B(\omega)e^{2i\delta(\omega,\tau)}}$$

Here, $\tilde{\mathrm{r}}_A(\omega,\tau)$ and $\tilde{\mathrm{r}}_B(\omega,\tau)$ are the reflection coefficients at the interfaces vacuum/photoexcited layer and photoexcited layer/unperturbed bulk, respectively, while $\delta = 2\pi d\tilde{n}(\omega,\tau)/\lambda_0$, with $\tilde{n}(\omega,\tau)$ being the complex refractive index of the photo-excited layer and λ_0 the probe wavelength.

Numerically solving this equation allowed us to retrieve $\tilde{n}(\omega,\tau)$ from the reflection coefficient $\tilde{\mathrm{r}}(\omega,\tau)$ obtained in the experiment. The complex optical conductivity for the homogeneously excited volume of the material is expressed as $\tilde{\sigma}(\omega,\tau) = \frac{\omega}{4\pi i}[\tilde{n}(\omega,\tau)^2 - \varepsilon_\infty]$, with $\varepsilon_\infty = 4.5$ as a standard value for high-T_C cuprates.

In Figure S2.1 & S2.2 we report, for specific data sets, all the individual steps involved in the determination of the transient optical response functions.

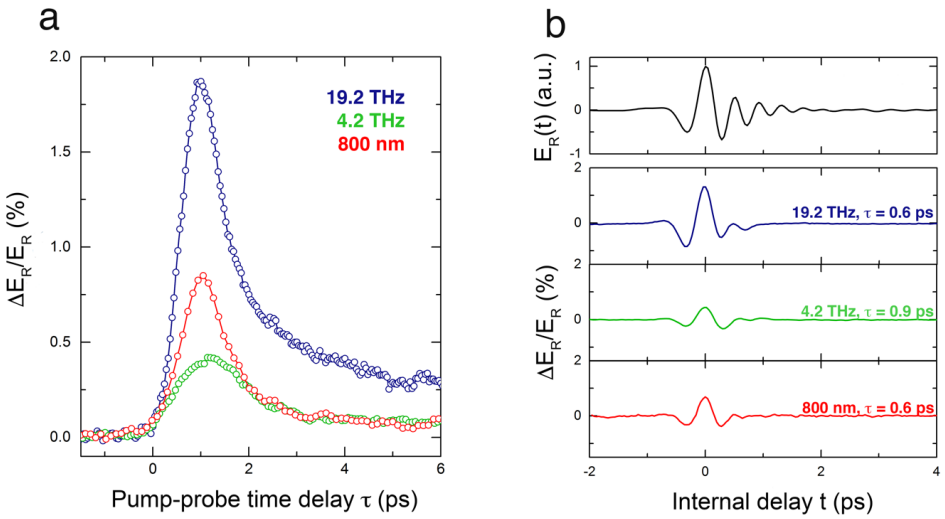

Figure S2.1. a. Raw pump-induced changes at the peak of the THz probe electric field (internal delay $t = 0$) as a function of pump-probe delay τ, measured in $YBa_2Cu_3O_{6.5}$ at T = 100 K for excitation at $\omega_{pump} = 4.2$ THz (green), $\omega_{pump} = 19.2$ THz (blue), and $\lambda_{pump} = 800$ nm (red). **b**. Top panel: Electro-optic sampling scan of the stationary THz probe electric field profile, $E_R(t)$, reflected from the sample. Lower panels: Transient scans of the pump-induced changes in $E_R(t)$, measured for the same pump frequencies as in panel (a), at a selected pump-probe time delay, τ.

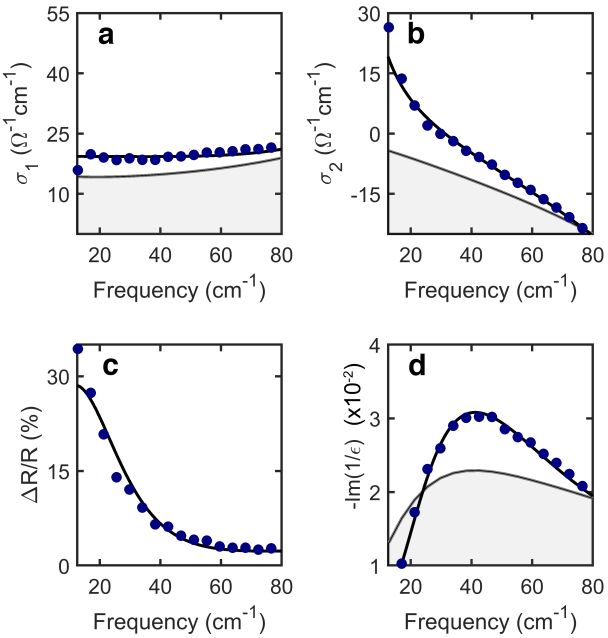

Figure S2.2. Real and imaginary part of the optical conductivity (**a, b**), relative changes in the reflectivity (**c**) and in the loss function (**d**), calculated for a homogeneously excited volume from the raw data of Fig. S2.1 ($\omega_{pump} = 19.2$ THz, time delay τ = 0.6 ps), using the penetration depth mismatch model described in the text (blue circles). Black lines are fits to the transient spectra (see Section S5), while grey lines indicate the same quantities measured in equilibrium.

S3. Equilibrium optical properties

The equilibrium optical properties of $YBa_2Cu_3O_{6.5}$ were determined following the same procedure described in Refs. 4 & 5.

The stationary reflected electric field, $E_R(t)$, was measured with the time-domain THz spectroscopy setup described in Sections S1 & S2, at different temperatures below and above T_C = 52 K. This was then Fourier transformed to obtain the complex-valued, frequency dependent $\tilde{E}_R(\omega)$.

The equilibrium reflectivity in the superconducting state, $R(\omega, T < T_C)$, was determined as $R(\omega, T < T_C) = \frac{|\tilde{E}_R(\omega, T<T_C)|^2}{|\tilde{E}_R(\omega, T \gtrsim T_C)|^2} R(\omega, T \gtrsim T_C)$. Here, $R(\omega, T \gtrsim T_C)$ is the normal-state reflectivity measured with Fourier-transform infrared spectroscopy [7], which is weakly frequency and temperature dependent in the THz range. An example of this procedure is shown in Fig. S3.1.

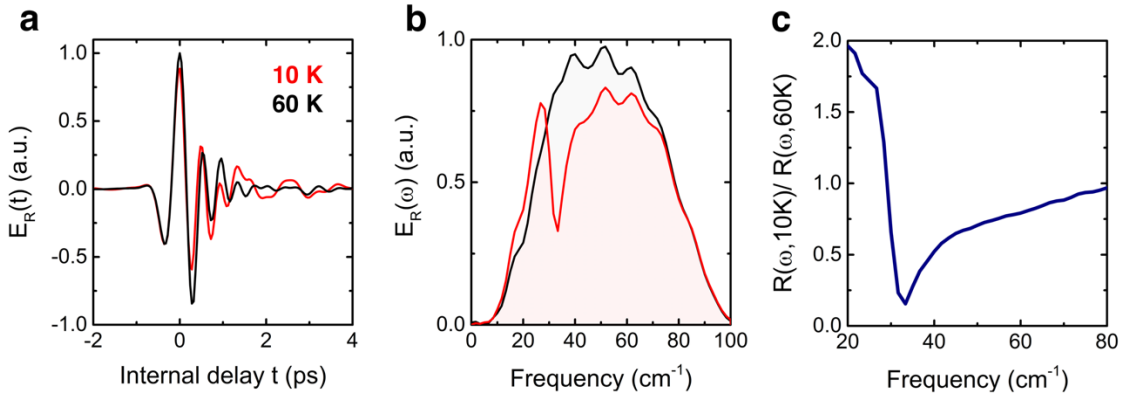

Figure S3.1. **a**. Stationary electric field profile measured after reflection from $YBa_2Cu_3O_{6.5}$ at $T < T_C$ (red) and $T = 60\ K \gtrsim T_C$ (black). **b**. Fourier transform amplitude of both quantities shown in panel a. **c**. Reflectivity ratio extracted from the spectra in panel (b), showing a Josephson Plasma Resonance at $\omega \simeq$ 35 cm^{-1}, in agreement with literature data [7].

These THz-frequency reflectivities were then fitted with the same models discussed in Section S5 (Josephson Plasma and Drude-Lorentz models for below-T_C and above-T_C data, respectively) and merged at $\omega \simeq 80$ cm^{-1} with the broadband spectra from Refs. [7,8,9]. This allowed us to perform Kramers-Kronig transformations, thus retrieving full sets of equilibrium optical response functions (*i.e.*, complex optical conductivity $\tilde{\sigma}_0(\omega)$, complex dielectric function $\tilde{\varepsilon}_0(\omega)$, complex refractive index $\tilde{n}_0(\omega)$) for all temperatures investigated in our pump-probe experiment. In Figure S3.2 we report selected quantities obtained with this procedure.

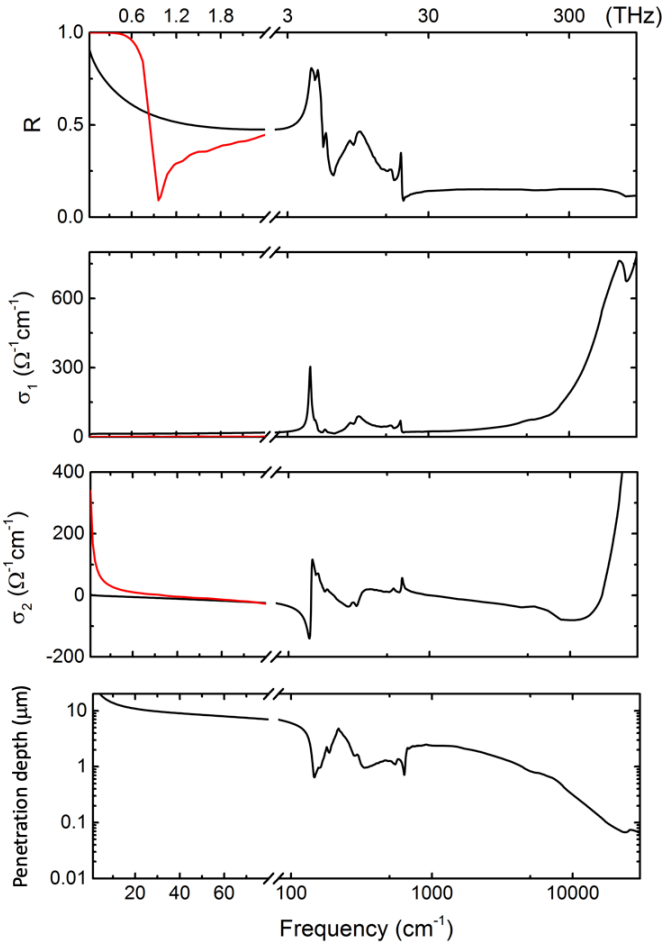

Figure S3.2. Equilibrium reflectivity, complex optical conductivity and penetration depth, $d(\omega) = \frac{c}{2\omega \cdot \mathrm{Im}[\tilde{n}_0(\omega)]}$, of $YBa_2Cu_3O_{6.5}$ at T = 100 K (black curves), extracted with the procedure described in the text. Red lines refer to below T_C data (T = 10 K).

S4. Uncertainties in the determination of the transient optical properties

We examine here different sources of uncertainty and their propagation in the data analysis. We choose to apply this examination to a representative data set taken at T = 100 K for narrowband excitation at 19.2 THz.

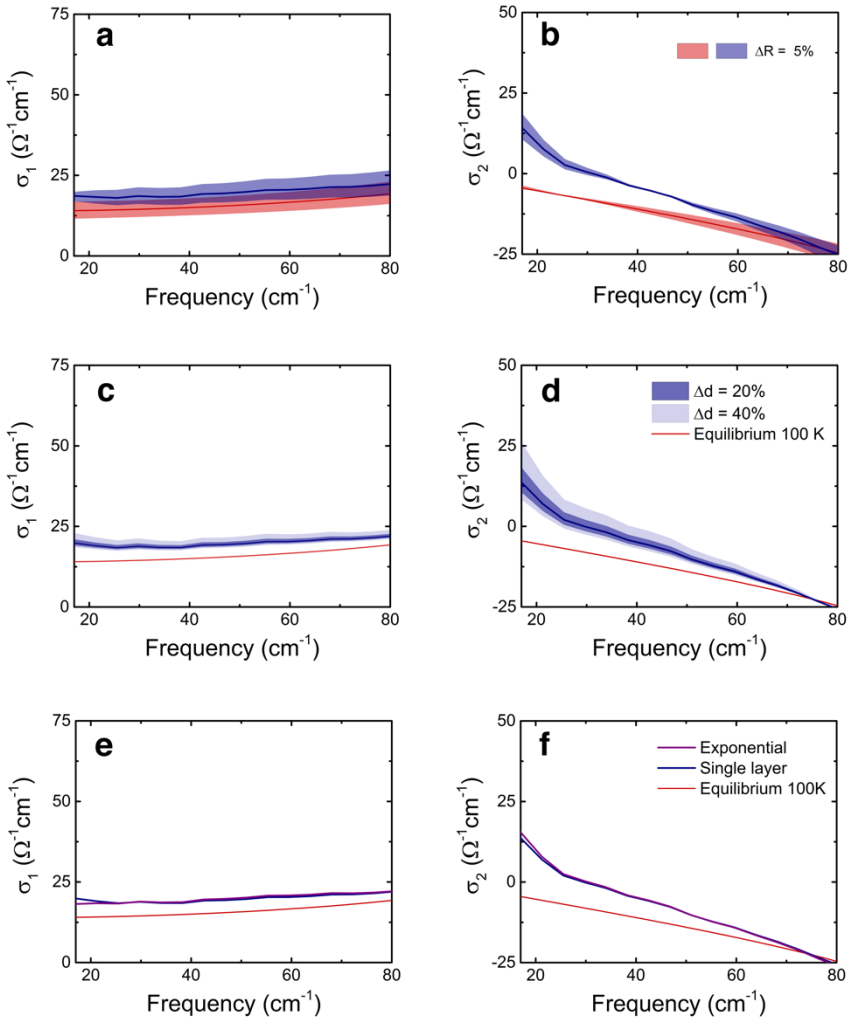

Figure S4. Effects of different sources of uncertainties in the determination of the transient optical conductivity of $YBa_2Cu_3O_{6.5}$ at T = 100 K and $\tau = 0.6$ ps time delays after narrowband excitation at 19.2 THz. In all panels, equilibrium values are shown in red, while transient spectra are in blue. Error bars, displayed as colored bands, have been propagated as follows: **a-b**, ±5% uncertainty in the equilibrium R(ω); **c-d**, ±20% and ±40% change in the pump penetration depth d= 0.7 μm. In **e-f** we analyze the effect of different functional forms for modelling the pump–probe penetration depth mismatch: a single-layer model, or a multi-layer model with exponential profile, both with the same pump penetration depth d= 0.7 μm.

The typical uncertainty in the absolute value of the measured equilibrium reflectivity is of the order of ±2-3%. Figure S4a-b shows as colored bands the propagated error bars in the equilibrium and transient optical properties for a ±5% uncertainty in R(ω). The response appears to be only marginally affected.

Another possible source of error resides in the value of the pump penetration depth used in the layered-system analysis to determine the transient response of a homogeneously excited volume. For 19.2 THz, this value was set to d= 0.7 μm. In Fig. S4c-d we show how a ±20% and a ±40% change in the pump penetration depth would affect the transient optical properties.

Finally, in Fig. S4e-f we show the effect of a different choice of the model for describing the pump probe penetration depth mismatch. The "single" photoexcited layer description, used for all data analyzed in the paper and described in Section S2, is compared with an exponential "multi-layer" decay model (used, for example, in Ref. [5]). Importantly, in all cases considered here, the impact of the different sources of error on the calculated optical conductivities is negligible.

S5. Fitting models

At each pump probe time delay τ, the transient *c*-axis optical response functions were fitted either with a model including the response of a Josephson plasma or with a simple Drude-Lorentz model for normal conductors [6]. A single set of fit parameters was always used to simultaneously reproduce the real and imaginary part of the optical conductivity, $\sigma_1(\omega)$ and $\sigma_2(\omega)$.

The phonon modes in the mid-infrared (150 cm^{-1} $\lesssim \omega \lesssim$ 700 cm^{-1}) and the high-frequency electronic absorption ($\omega \gtrsim$ 3000 cm^{-1}) were constructed by fitting the equilibrium spectra with Lorentz oscillators, for which the complex dielectric function is expressed as:

$$\tilde{\varepsilon}_{HF}(\omega) = \sum_i \frac{S_i^2}{(\Omega_i^2 - \omega^2) - i\omega\Gamma_i}.$$

Here, Ω_i, S_i, and Γ_i are the central frequency, strength, and damping coefficient of the *i*-th oscillator, respectively. In all fitting procedures to the transient data, these high-frequency terms were kept fixed.

The low-frequency Drude contribution to the complex dielectric function is expressed as

$$\tilde{\varepsilon}_D(\omega) = \varepsilon_\infty - \omega_P^2/(\omega^2 + i\Gamma\omega),$$

where ω_P and Γ are the Drude plasma frequency and momentum relaxation rate, which were left as free fitting parameters, while ε_∞ was kept fixed to 4.5.

The dielectric function of the Josephson plasma is expressed instead as

$$\tilde{\varepsilon}_J(\omega) = \varepsilon_\infty - \omega_J^2/\omega^2 + \tilde{\varepsilon}_N(\omega).$$

Here, the free fit parameters are the Josephson plasma frequency, ω_J, and $\tilde{\varepsilon}_N(\omega)$, a weak "normal fluid" component [6,10] (overdamped Drude term), which was introduced to reproduce the positive offset in $\sigma_1(\omega)$.

As an example, Figure S5 reports the photo-induced optical conductivity for 19.2 THz narrowband excitation at different time delays τ = 0.6 ps and 2.4 ps and the corresponding fits. At early time delay (τ = 0.6 ps), the Josephson plasma model (black solid lines) is able to reproduce the experimental data. Notably, a Drude response alone (dashed lines) would not capture the measured low-frequency increase in $\sigma_2(\omega)$.

At later time delays (Fig. S5b), for which the system has already evolved into a dissipative response, the experimental data could instead be well reproduced by the simple Drude model for normal conductors.

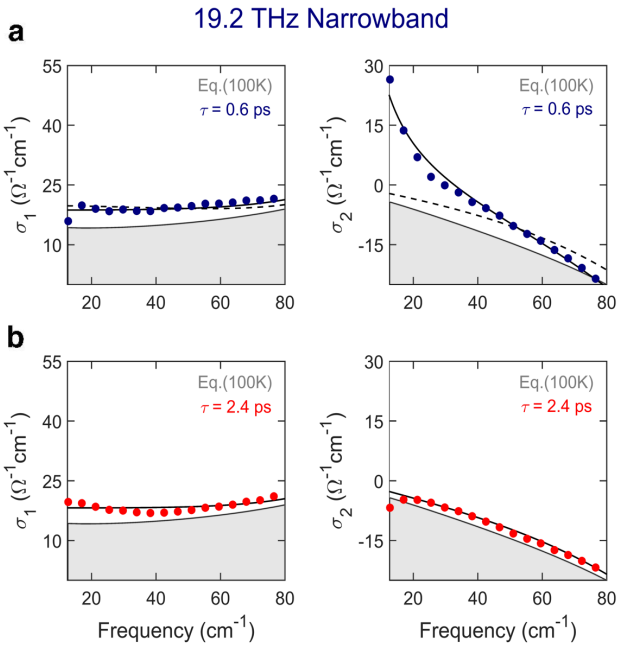

Figure S5. Fits to the transient complex optical conductivity measured after narrowband excitation at ω_{pump} = 19.2 THz (T = 100 K). **a.** Real and imaginary part of the optical conductivity measured at τ = 0.6 ps pump-probe time delay (blue dots). Grey curves with shading are the corresponding equilibrium spectra (shown also in panels b). The black solid line is a fit with the Josephson plasma model. The dashed black curve is instead a failed fit attempt using a simple Drude term for normal conductors. **b.** Real and imaginary conductivity measured at τ = 2.4 ps time delay (red dots). This dissipative response could be well reproduced by the Drude-Lorentz model (black solid lines).

S6. Extended data sets

The full dynamical evolution of the photoinduced changes in the complex optical conductivity at $T = 100\ K \gg T_C$, which is reported in Fig. 2 of the main text for both broadband and narrowband excitation at 19.2 THz, is shown here also for narrowband excitation at 16.4 THz (Fig. S6.1), 4.2 THz, and 10.1 THz (Fig. S6.2).

For each data set, we display color plots of the real and imaginary part of the optical conductivity as a function of both frequency and pump-probe time delay, along with

selected spectra measured at the peak of the response (in analogy with Fig. 2 in the main text). In addition, we plot two frequency-integrated quantities as a function of time delay: $\omega\sigma_2(\omega)|_{\omega\to 0}$, which in a superconductor is proportional to the superfluid density, and $\int \Delta\sigma_1(\omega)d\omega$, which is a reporter of dissipation and quasiparticle heating inside the gap.

As already extensively discussed in the main text, only driving at the two high-frequency modes at 16.4 THz and 19.2 THz induced a superconducting-like response ($\sigma_2(\omega) \propto 1/\omega$), for which the transient complex conductivity was fitted by a model describing the optical response of a Josephson plasma. On the other hand, excitation of the two low-frequency modes (at 4.2 THz and 10.1 THz) caused a moderate increase in dissipation and no superconducting component. This observation could be well reproduced, for all time delays, by a simple Drude-Lorentz model for normal conductors.

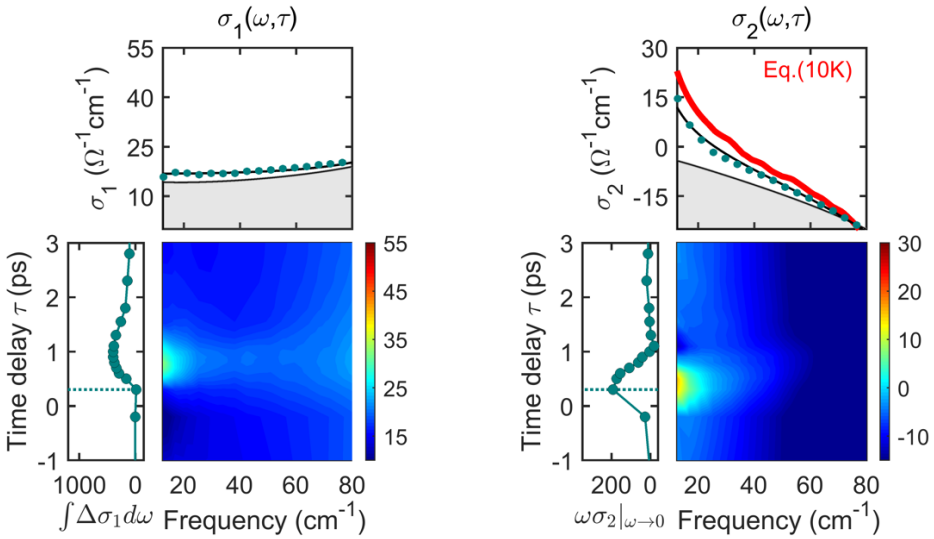

Figure S6.1. Frequency- and time-delay-dependent complex optical conductivity measured at T = 100 K for narrowband excitation at 16.4 THz (color plots). Upper panels: corresponding $\sigma_1(\omega)$ and $\sigma_2(\omega)$ line cuts displayed at equilibrium (grey lines) and at the time delay corresponding to the peak of the coherent response (teal circles). Black lines are fits to the transient spectra with a model describing the response of a Josephson plasma. For comparison, we also report the equilibrium $\sigma_2(\omega)$ measured in the superconducting state at T = 10 K (red line). Side panels: Frequency-integrated dissipative ($\int \Delta\sigma_1(\omega)d\omega$) and coherent ($\omega\sigma_2(\omega)|_{\omega\to 0}$) responses, as a function of pump-probe time delay. The delay corresponding to the spectra reported in the upper panels is indicated by a dashed line.

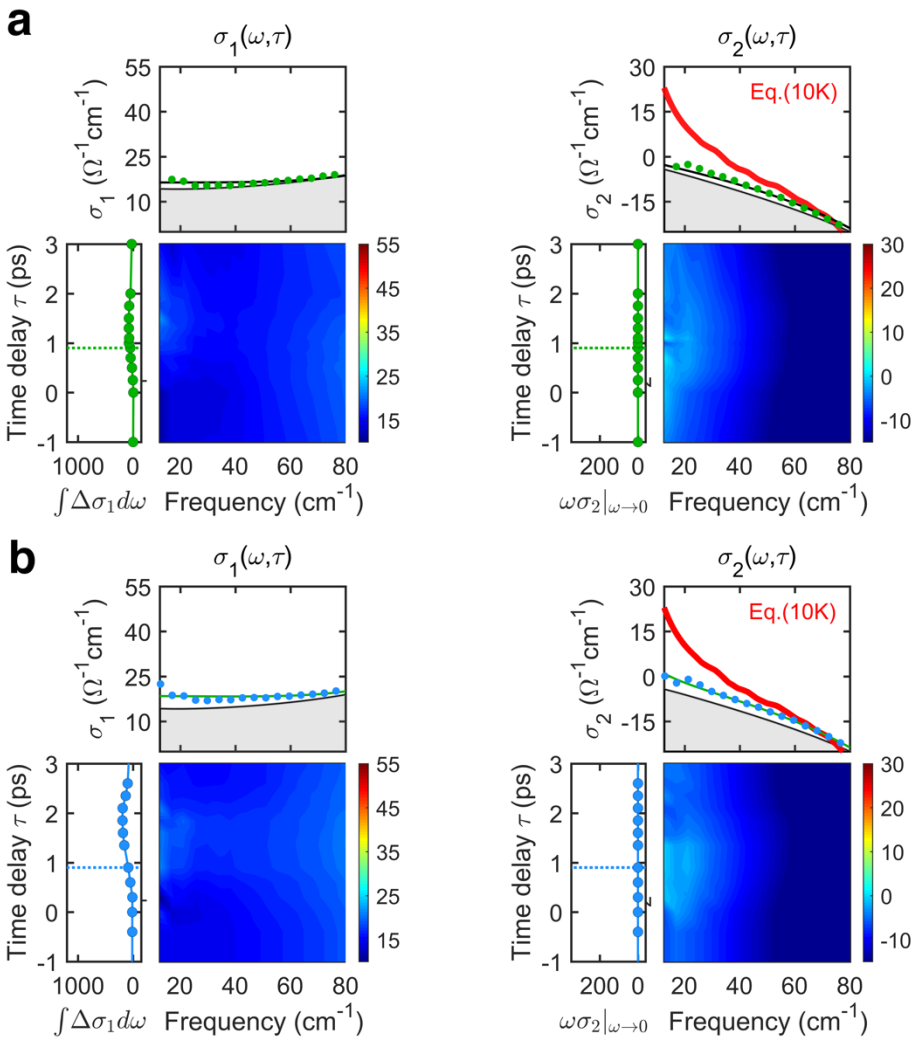

Figure S6.2. **a.** Frequency- and time-delay-dependent complex optical conductivity measured at T = 100 K for narrowband excitation at 4.2 THz (color plots). Upper panels: corresponding $\sigma_1(\omega)$ and $\sigma_2(\omega)$ line cuts displayed at equilibrium (grey lines) and at the time delay corresponding to the peak of the response (green circles). Black lines are fits to the transient spectra with a Drude-Lorentz model. For comparison, we also report the equilibrium $\sigma_2(\omega)$ measured in the superconducting state at T = 10 K (red line). Side panels: Frequency-integrated dissipative ($\int \Delta\sigma_1(\omega)d\omega$) and coherent ($\omega\sigma_2(\omega)|_{\omega\to 0}$) responses, as a function of pump-probe time delay. The delay corresponding to the spectra reported in the upper panels is indicated by a dashed line. **b.** Same quantities as in (a), measured for narrowband excitation at 10.1 THz.

In another set of experiments, we have also investigated the low-frequency THz response of $YBa_2Cu_3O_{6.5}$ for excitation above the phonon resonances, up to the near-infrared and visible spectral range.

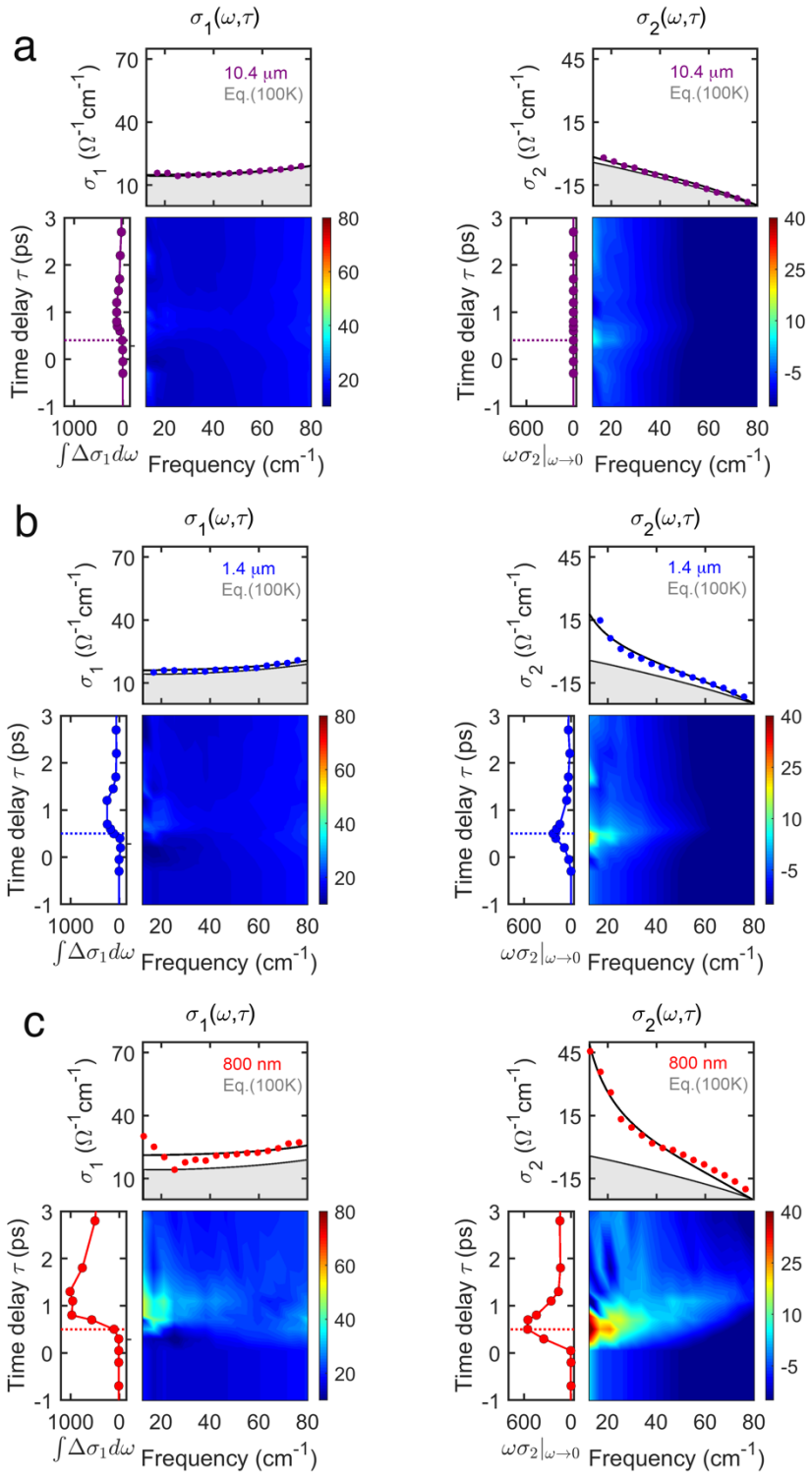

Figure S6.3. **a.** Frequency- and time-delay-dependent complext optical conductivity measured at T = 100 K for excitation at 10.4 μm (color plots). Upper panels: corresponding $\sigma_1(\omega)$ and $\sigma_2(\omega)$ line cuts displayed at equilibrium (grey lines) and at the time delay corresponding to the peak of the response (purple circles). Black lines are fits to the transient spectra with a Drude-Lorentz model. Side panels: Frequency-integrated dissipative ($\int \Delta\sigma_1(\omega)d\omega$) and coherent ($\omega\sigma_2(\omega)|_{\omega\to 0}$) responses, as a function of pump-probe time delay. The delay corresponding to the spectra reported in the upper panels is indicated by a dashed line. **b-c.** Same quantities as in (a), measured for excitation at 1.4 μm and 800 nm.

The transient complex conductivity measured at the peak of the light-induced response for three selected excitation frequencies, 29 THz ($\lambda_{pump} = 10.4$ μm), 214 THz ($\lambda_{pump} = 1.4$ μm), and 375 THz ($\lambda_{pump} = 800$ nm), is reported in Fig. 6 of the main text.

The full dynamical evolution of the photoinduced changes in the complex optical conductivity for these three excitation wavelengths and a fixed excitation fluence of ~8 mJ/cm^2 is shown here in Figs. S6.3. For each data set, we display the same quantities as in Figs. S6.1 and S6.2.

Remarkably, whilst the response to 10.4 μm driving is marginal, excitation at the two highest frequencies induces a transient optical conductivity compatible with dissipation-less transport ($\sigma_2(\omega) \propto 1/\omega$), strongly resembling that induced by driving resonant with the apical oxygen phonons (see also the discussion in the main text).

S7. Pump electric field dependence

In Figure S7 we report the dependence of the coherent component of the pump-induced response, $\omega\sigma_2(\omega)|_{\omega\to 0}$, on the driving peak electric field. These data are taken for narrowband apical oxygen driving at 19.2 THz, at T = 100 K. The linear electric field dependence, without any signature of saturation, confirms and extends the results reported in Ref. 5.

All data reported in Figs. 2,3,4,5 of the main text have been taken at the maximum electric field of ~3 MV/cm, corresponding to a pump fluence of ~8 mJ/cm^2.

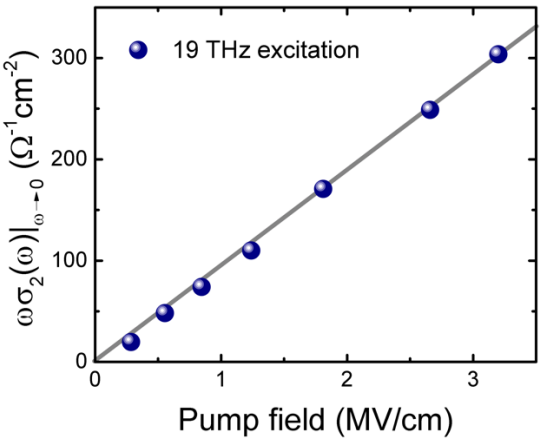

Figure S7. Pump electric field dependence of the coherent component of the light-induced response, represented by the low-frequency limit $\omega\sigma_2(\omega)|_{\omega\to 0}$, measured in $YB_2Cu_3O_{6.5}$ at 100 K after photo-excitation with narrowband pulses at 19.2 THz.

S8. Transient response below T_C

The transient response in the superconducting state of $YBa_2Cu_3O_{6.5}$ was investigated at $T = 10$ K for the same excitation frequencies, 4.2 THz and 19.2 THz, for which we have reported the temperature dependent response in Fig. 5 of the main text.

In Figure S8 we report the dynamical evolution of the real and imaginary part of the complex optical conductivity for 4.2 THz driving at ~8 mJ/cm^2 fluence, 19.2 THz driving at ~8 mJ/cm^2 fluence, and 19.2 THz driving at ~1.5 mJ/cm^2 fluence.

For apical oxygen excitation at 19.2 THz with high fluence (middle panel) we observe an analogous response to that reported previously [4,5], namely a short-lived enhancement in the $\sigma_2(\omega)$ divergence after photo-excitation, accompanied by a weak offset in $\sigma_1(\omega)$. This behavior is indicative of a transient increase in superfluid density, which (in analogy with the observation above T_C) appears to be stronger than in previous experiments due to the higher available pump fluence.

If the same experiment is repeated at a lower pump fluence (right panel), comparable to that employed in Ref. 11, only a transient depletion of the superconducting condensate is observed.

Finally, for 4.2 THz pump (left panel) a similar depletion and no enhancement is found for any driving field, a result which shall be related to the absence of any light-induced coherence above T_C at this excitation frequency (see Figs. 3 & 4 of main text).

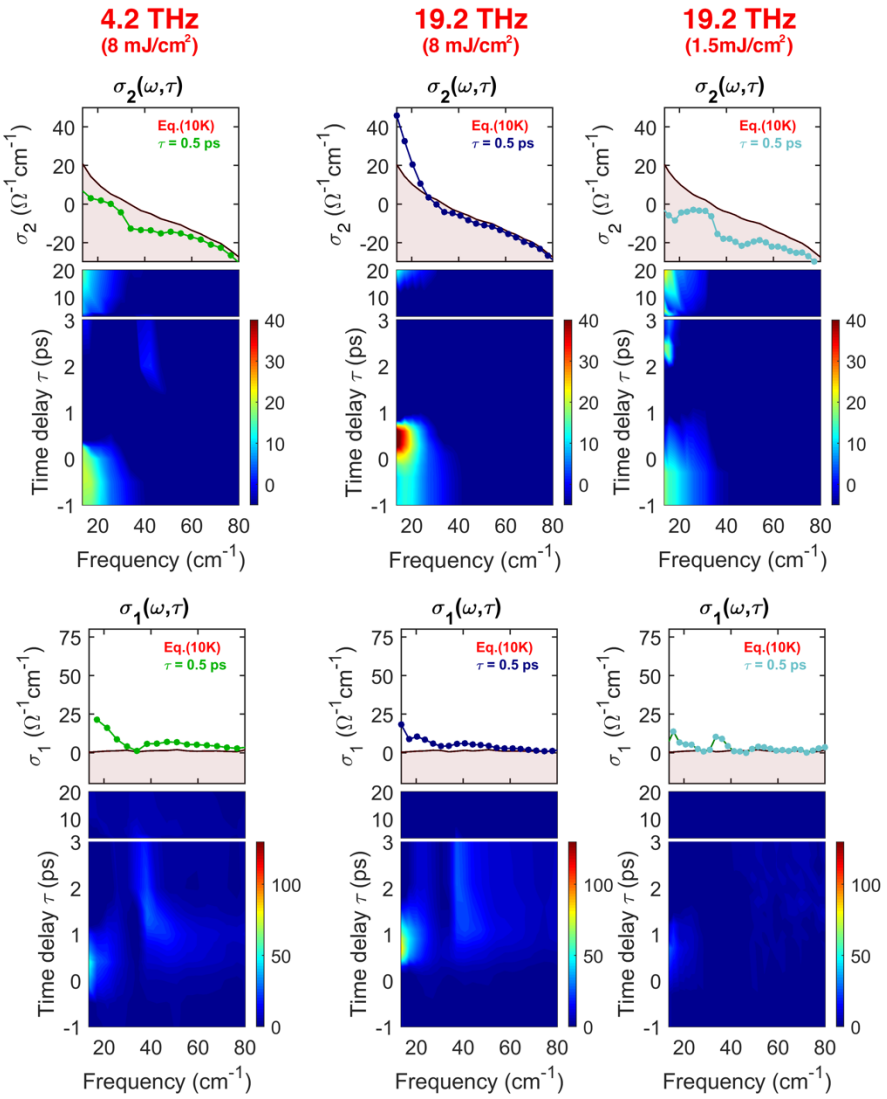

Figure S8. Frequency- and time-delay-dependent real and imaginary part of the optical conductivity measured in $YBa_2Cu_3O_{6.5}$ at T = 10 K for narrowband excitation at 4.2 THz (left panel) and 19.2 THz (at two pump fluences, center and right panels). Upper panels: corresponding line cuts displayed at equilibrium (grey lines) and at the time delay corresponding to the peak of the response (colored circles).

S9. Pump-induced heating

Following the procedure described in Ref. 12, we have used a two-temperature model to estimate the lattice temperature after electron-phonon thermalization, induced by photoexcitation at two different pump frequencies.

The specific heat for $YBa_2Cu_3O_{6.5}$ is described by the relation $C_S = \gamma T + \beta T^3$ over a wide temperature range, where $\gamma \simeq 2.3$ mJ/mol^{-1}K^{-2} and $\beta \simeq 0.394$ mJ/mol^{-1}K^{-4} are the electronic and lattice coefficients to the specific heat estimated from literature [13], respectively.

For a given pump fluence, we calculated the absorbed energy over the photo-excited region and determined the effective temperature after electron phonon-thermalization by integrating $Q_{pump} = \int_{T_i}^{T_f} NC_S(T)dT$, where Q_{pump} is the total energy absorbed from the pump pulse, N is the number of moles in the excited volume, T_i is the initial temperature and T_f the temperature after electron-phonon thermalization. The absorbed energy was estimated by $Q_{pump} = FA(1-R)$, where F is the pump fluence, A is the area of the pump beam on the sample, and R is the reflectivity at the pump frequency. The excited volume was calculated as a cylindrical disk with a diameter of ~400 μm and height equal to the pump penetration depth.

The final temperature, T_f, is plotted versus pump fluence in Fig. S9 for an initial temperature T_i = 100 K. The colored circles correspond to the highest fluence used in our experiment, for which the pump-induced heating is limited to below ~20 K.

We stress here that our paper focuses on the analysis of early time delay dynamics ($\tau \lesssim 3$ ps), for which full thermalization has certainly not occurred yet [14]. The calculation

reported here is relevant for dynamics at longer time delays, which is not the main subject of the present work.

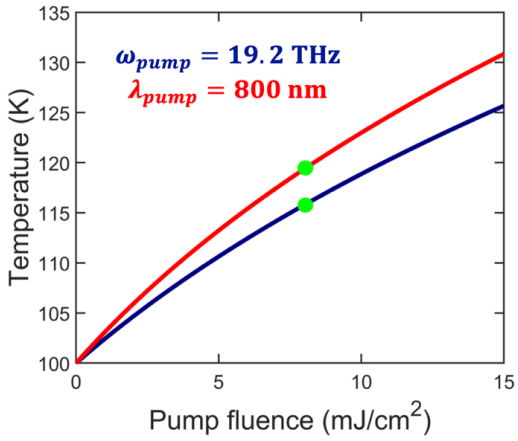

Figure S9. Calculated final lattice temperature after electron-phonon thermalization as a function of excitation fluence for 19 THz (blue) and 800 nm pump (red). The same approach reported in Ref. 12 has been applied. The maximum pump fluence used in our experiment is indicated by green dots.

S10. Ab-initio calculations of the structural dynamics

In this Section, we correlate the experimentally-determined frequency band for the stimulation of transient superconductivity with the optically-driven rearrangement of the crystal structure, which we calculated by combining effective Hamiltonian modeling with first-principle computations.

Our approach is based on an anharmonic crystal potential that consists of three distinct contributions [15,16,17]:

1. The harmonic potential of each phonon mode

$$V_{harm} = \sum \frac{\omega_i^2}{2} Q_i^2, \qquad \text{(S10.1)}$$

with ω_i and Q_i representing the eigenfrequency and coordinate of the i-th mode, respectively.

2. The anharmonic potential containing higher-order terms of the phonon coordinates and combinations of different phonon modes

$$V_{anharm} = \sum g_{ijk} Q_i Q_j Q_k + \sum f_{iklm} Q_i Q_k Q_l Q_m, \quad \text{(S10.2)}$$

with g_{ijk} and f_{iklm} indicating third and fourth order anharmonic coefficients, respectively.

3. The coupling of each individual phonon mode to an external electric field

$$V_{efield} = \sum Z_i^* Q_i E_{field}\,, \quad \text{(S10.3)}$$

with Z_i^* representing the mode effective charge [18,19].

The structural dynamics are then determined by the equations of motion for each phonon mode, given by

$$\ddot{Q}_i + 2\gamma_i \dot{Q}_i + \nabla_{Q_i}\left(V_{harm} + V_{anharm} + V_{efield}\right) = 0. \quad \text{(S10.4)}$$

Here, we introduced a phenomenological damping term γ_i, which accounts for contributions to the finite lifetime which are not already considered within the anharmonic potential. Importantly, the equations are restricted to phonon modes at the Brillouin zone center, due to the long wavelengths of the THz excitation pulses.

Various studies have shown that this approach is able to describe the structural dynamics induced by the resonant excitation of infrared-active modes in a solid [20,21]. However, only a small subset of all possible phonon coupling constants was considered in these

cases, predominantly due to computational limitations. In the present simulations, this reduction was overcome by utilizing the approaches given in Refs. [15,22]. We list all technical and numerical details at the end of this Section.

We simulated the THz-driven structural dynamics of the ortho-II structure of $YBa_2Cu_3O_{6.5}$, which exhibits 73 non-translational phonon modes at the Brillouin zone center. The most relevant phonon modes for *c*-axis polarized THz excitation are 13 B_{1u} modes, which exhibit a finite electric dipolar moment along this direction. In addition, there are 11 A_g modes, which fulfill the symmetry requirements to exhibit a finite third-order type coupling to the B_{1u} modes [15,20]. A full list of the eigenfrequencies of these modes is presented at the end of this Section.

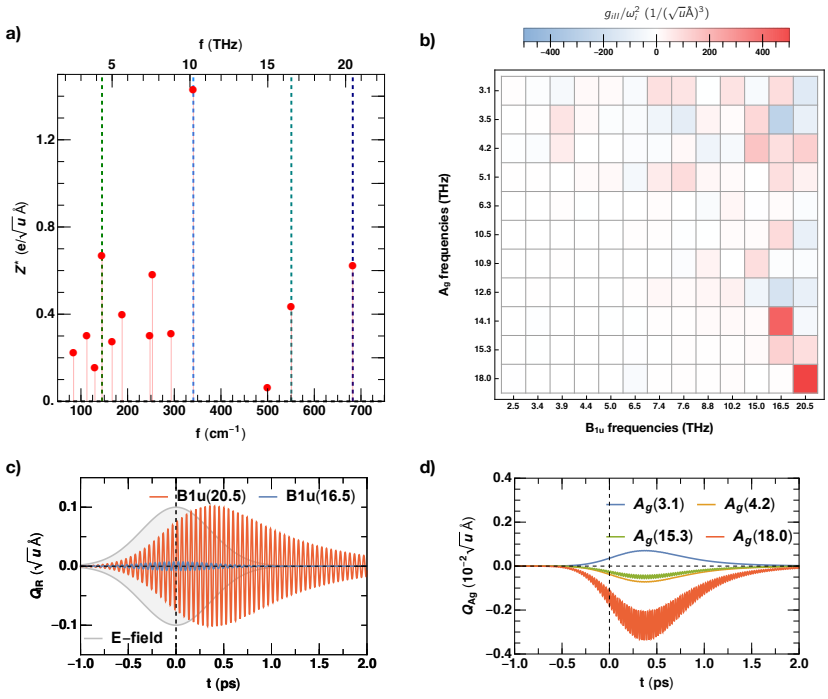

Figure S10.1. **a.** Mode effective charges for the polar B_{1u} modes of the $YBa_2Cu_3O_{6.5}$ ortho-II structure. **b.** Third-order anharmonic coupling coefficients of the type $Q_{Ag}Q_{IR}^2$ for all B_{1u} and A_g modes. **c.** Oscillations of two B_{1u} modes at 16.5 and 20.5 THz driven by a narrowband THz pulse at 20.5 THz (grey area). **d**. Dynamics of the four A_g modes exhibiting stronger coupling to the 20.5-THz B_{1u} mode driven in panel c.

The calculated effective charges for the B_{1u} modes, needed to describe their excitation by a THz electric field according to Eq. (S10.3), are shown in Figure S10.1a. We assumed here that the Born effective charge of each atom equals its ionic charge. In agreement with experimental observations [23], we obtain large values for the two highest-frequency apical-oxygen modes at 16.5 THz and 20.5 THz, for the 10-THz mode affecting the CuO_2 layers, and for the mode at 4 THz that involves Ba displacements. Note also that all phonon frequencies match within a few percent the values determined from the experiment.

Group symmetry dictates three sets of third-order couplings for the phonon modes considered. The first is the coupling of the square of the optically-excited B_{1u} modes to a single A_{1g} mode, proportional to $Q_{IR,i}^2 Q_{Ag}$. The second is the coupling of two different B_{1u} modes to a single A_{1g} mode ($Q_{IR,i} Q_{IR,j} Q_{Ag}$), and the third is the coupling between three A_{1g} modes ($Q_{Ag,i} Q_{Ag,j} Q_{Ag,k}$). For the fourth-order coupling terms, we only considered the terms of the form Q_i^4 and neglected expressions mixing two or more phonon modes. Thus, we took into account, in total, 1067 third-order and 24 fourth-order coupling coefficients. Note that, in the earlier studies of Refs. [15,20], at maximum 24 coupling coefficients were considered. As an example, Figure S10.1b shows a subset of the computed anharmonic coupling coefficients, representing the two-mode coupling of the type $Q_{IR,i}^2 Q_{Ag}$. Both the two highest-frequency B_{1u} polar modes couple strongly to two different A_{1g} modes, similar to the observations reported for $YBa_2Cu_3O_7$ in Ref. [15].

Figure S10.1c,d show the dynamics of two selected B_{1u} modes and four anharmonically coupled A_g modes. The time traces have been triggered by an electric field pulse $E(t) = e^{\frac{2t^2 ln(2)}{FWHM^2}} cos(\omega t)$ with a 3 MV/cm peak field and 0.6 ps pulse duration (FWHM) at 20.5 THz. The resonantly excited 20.5-THz B_{1u} mode oscillates with an amplitude that is about one order of magnitude larger than that of the off-resonant B_{1u} mode at 16.5 THz. The

dominant A_g modes, anharmonically coupled to the B_{1u} phonons, are transiently displaced from their equilibrium positions with significant amplitudes ($|Q_{Ag}| < 10^{-5}\sqrt{u}$Å). They reach their maximum displacements at about 0.4 ps time delay, for which also the resonantly driven 20.5-THz B_{1u} mode reaches its peak amplitude.

In the same way, we constructed the time dependent crystal structures for different excitation frequencies between 2.5 and 22 THz and focused on the transient displacements of A_g modes, which involve an average distortion of the crystal lattice [15,20]. Figure S10.2 shows the maximum changes of selected bonds (distance of the apical oxygen atoms from the CuO_2 planes, inter-bilayer distance of the CuO_2 planes, and buckling of the CuO_2 planes) calculated from these average phonon displacements. Peak electric field and pulse duration were kept fixed at 3 MV/cm and 0.6 ps, respectively, for all driving frequencies.

For excitation in the interval between 5 and 10 THz, we observed a significant shift of the apical oxygen atoms closer to the CuO_2 planes, accompanied by a buckling within the CuO_2 layers and an increase in the intra-bilayer distance. In contrast, very different rearrangements were found for driving frequencies within the range for which photo-induced superconducting coherence was observed. Most prominently, the apical oxygen atoms moved away from the CuO_2 planes for resonant driving of the 20.5-THz phonon, while excitation of the 16.5-THz mode shifted the atoms closer to the planes. In both cases, we also calculated different signs for the CuO_2 plane buckling and the intra-bilayer distance, which increased for 16.5-THz but decreased for the 20.5-THz excitation.

Overall, we did not find a consistent trend in the transient crystal structures, which was unique to the frequency band for which transient superconductivity was observed. As such, this result puts some doubts on the significance of anharmonic phonon coupling as

a possible mechanism for optically-driven superconductivity in $YBa_2Cu_3O_{6+x}$, as posited earlier in Ref. [20].

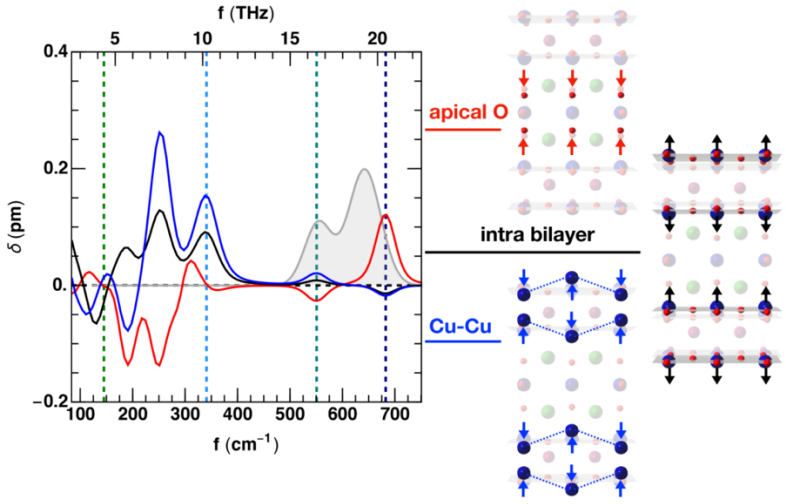

Figure S10.2. Transient average distortions of the apical oxygen positions (red), the intra-bilayer distance (black) and the planar Cu buckling (blue) in $YBa_2Cu_3O_{6.5}$, derived from ab-initio calculations of nonlinear phonon-phonon interactions for different excitation frequencies. The grey shaded area depicts the experimentally determined frequency range of the optically-enhanced superconducting response shown in Figure 4 of the main text. The excitation parameters of 600 fs pulse duration and 3 MV/cm peak electric field, used in the calculations, reproduce the experimental conditions. Arrows in the illustrations shown on the right correspond to positive displacements.

Technical and numerical approach for the ab-initio calculations:

We employed first-principles total energy calculations in the framework of the density functional theory (DFT) to compute all harmonic and anharmonic terms included in the equations (S10.1), (S10.2), and (S10.3). Specifically, we used the implantation of DFT, applying the linearized augmented-plane wave method (LAPW) within the ELK-code [24]. We approximated the exchange-correlation functional by the local density approximation. In addition, we performed careful tests of all relevant numerical parameters entering the computation. The setting for well-converged results corresponded to a truncation at l_{max}=10 of the angular expansion of wave functions and potential within the muffin-tin radii (2.6, 2.8, 1.85 and 1.4 a.u. for Y, Ba, Cu, and O, respectively). A $|G|_{max}$=20 a.u.$^{-1}$ limited

the potential and density expansion within the interstitial region. We set $R_{MT} \times k_{max}$=8.0 for truncating the plane-wave wavefunction expansion. The Brillouin zone was sampled within our computations by a 11×19×5 k-point mesh. The same configuration was also employed in a previous study [25] and, within this setting, the forces (most relevant for phonons and anharmonic terms) were made to converge by less than 0.1 meV/Å.

Before computing the coefficients of the anharmonic potential, we first structurally relaxed the unit cell of $YBa_2Cu_3O_{6.5}$, for which we considered the ortho-II structure, following previous studies and the experimental setting [20]. As lowest energy state, we obtained the atomic configuration given in Table S10.1.

Finally, the phonon eigensystem was computed by frozen-phonon calculation using symmetry-adapted distortions generated with the Phonopy package [26]. We list all modes at the zone center in Table S10.2. Next, we applied the prescription in Ref. [22] to calculate the anharmonic constants of third order and took the approach of Ref. [15] for the quartic order terms.

Last, we computed the mode-effective charges appearing in equation (S10.3) by using the nominal averaged ionic charges of each atom as Born charges. Explicitly, we have for Yttrium 3+, Barium 2+, Copper 2+ and Oxygen 2-.

Table S10.1. DFT minimized structural configuration of the $YBa_2Cu_3O_{6.5}$ ortho-II cell with $a = 7.55$ Å, $b = 3.81$ Å, and $c = 11.50$ Å.

element	Wykoff position	*x*	*z*	element	Wykoff position	*X*	*z*
Y	l	0.251	0.500	O1	e	0.000	0.000
Ba	x	0.244	0.187	O2	w	0.250	0.378
Cu1	a	0.000	0.000	O3	r	0.000	0.378
Cu2	b	0.500	0.000	O4	t	0.500	0.378
Cu3	q	0.000	0.356	O5	q	0.000	0.161
Cu4	s	0.500	0.355	O6	s	0.500	0.153

Table S10.2. Computed DFT eigenfrequencies of the phonon modes at the center of the Brillouin zone for the $YBa_2Cu_3O_{6.5}$ ortho-II structure.

Label	f (THz)	Label	f (THz)	Label	f (THz)	Label	f (THz)
A_g	3.1	B_{1u}	7.4	B_{2u}	17.0	B_{3u}	8.1
A_g	3.5	B_{1u}	7.6	B_{2u}	17.4	B_{3u}	8.4
A_g	4.2	B_{1u}	8.8	B_{2g}	1.8	B_{3u}	10.3
A_g	5.1	B_{1u}	10.2	B_{2g}	2.6	B_{3u}	10.5
A_g	6.3	B_{1u}	15.0	B_{2g}	4.1	B_{3u}	11.8
A_g	10.5	B_{1u}	16.5	B_{2g}	4.2	B_{3u}	13.4
A_g	10.9	B_{1u}	20.5	B_{2g}	6.5	B_{3u}	18.3
A_g	12.6	B_{1g}	2.9	B_{2g}	7.4	B_{3g}	2.0
A_g	14.1	B_{1g}	3.8	B_{2g}	8.7	B_{3g}	4.1
A_g	15.3	B_{1g}	9.7	B_{2g}	10.0	B_{3g}	5.4
A_g	18.0	B_{2u}	2.4	B_{2g}	11.3	B_{3g}	6.5
A_u	2.8	B_{2u}	3.6	B_{2g}	11.4	B_{3g}	10.3
A_u	10.8	B_{2u}	4.7	B_{2g}	18.1	B_{3g}	11.1
B_{1u}	2.5	B_{2u}	5.2	B_{3u}	2.5	B_{3g}	16.6
B_{1u}	3.4	B_{2u}	5.6	B_{3u}	2.9	B_{3g}	17.2
B_{1u}	3.9	B_{2u}	8.0	B_{3u}	3.7		
B_{1u}	4.4	B_{2u}	10.3	B_{3u}	3.8		
B_{1u}	5.0	B_{2u}	11.5	B_{3u}	4.7		
B_{1u}	5.6	B_{2u}	16.6	B_{3u}	5.4		

References

[1] A. Sell, A. Leitenstorfer, and R. Huber, Opt. Lett. **33**, 2767 (2008).

[2] C. Manzoni, H. Ehrke, M. Först, and A. Cavalleri, Opt. Lett. **35**, 757 (2010).

[3] B. Liu, H. Bromberger, A. Cartella, T. Gebert, M. Först, and A. Cavalleri, Opt. Lett. **42**, 129 (2017).

[4] W. Hu, S. Kaiser, D. Nicoletti, C. R. Hunt, I. Gierz, M. C. Hoffmann, M. Le Tacon, T. Loew, B. Keimer, and A. Cavalleri, Nat. Mater. **13**, 705 (2014).

[5] S. Kaiser, C. R. Hunt, D. Nicoletti, W. Hu, I. Gierz, H. Y. Liu, M. Le Tacon, T. Loew, D. Haug, B. Keimer, and A. Cavalleri, Phys. Rev. B **89**, 184516 (2014).

[6] D. Nicoletti, D. Fu, O. Mehio, S. Moore, A. S. Disa, G. D. Gu, and A. Cavalleri, Phys. Rev. Lett. **121**, 267003 (2018).

[7] C. C. Homes, T. Timusk, D. A. Bonn, R. Liang, and W. N. Hardy, Physica C **254**, 265-280 (1995).

[8] E. Uykur, K. Tanaka, T. Masui, S. Miyasaka, and S. Tajima, Journal of Physical Society of Japan **81**, SB035 (2012).

[9] E. Uykur, "Pseudogap and precursor superconductivity study of $YBa_2(Cu_{1-x}Zn_x)_3O_y$: c-axis optical study from underdoped to overdoped region", Springer Japan (2015).

[10] D. van der Marel and A. Tsvetkov, Czech. J. Phys. **46**, 3165 (1996).

[11] S. J. Zhang, Z. X. Wang, H. Xiang, X. Yao, Q. M. Liu, L. Y. Shi, T. Lin, T. Dong, D. Wu, N. L. Wang, *arXiv:1904.10381* (2019).

[12] K. A. Cremin, J. Zhang, C. C. Homes, G. D. Gu, Z. Sun, M. M. Fogler, A. J. Millis, D. N. Basov, R. D. Averitt, *Proc. Natl. Acad. Sci. U.S.A*. **116**, 19875-19879 (2019).

[13] J. B. Kemper, Measurement of the heat capacity of cuprate superconductors in high magnetic fields. *Doctoral Thesis*, College of arts and science, Florida State University (2014).

[14] H. Niwa, N. Yoshikawa, K. Tomari, R. Matsunaga, D. Song, H. Eisaki, and R. Shimano, Phys. Rev. B **100**, 104507 (2019).

[15] M. Fechner and N. A. Spaldin, Phys. Rev. B **94**, 134307 (2016).

[16] A. Subedi, A. Cavalleri, and A. Georges, Phys. Rev. B **89**, 220301 (2014).

[17] D. M. Juraschek, M. Fechner, and N. A. Spaldin, Phys. Rev. Lett. **118**, 054101 (2017).

[18] X. Gonze and C. Lee, Phys. Rev. B **55**, 10355 (1997).

[19] A. Cartella, T. F. Nova, M. Fechner, R. Merlin, and A. Cavalleri, Proc. Natl. Acad. Sci. USA **115**, 12148 (2018).

[20] R. Mankowsky, A. Subedi, M. Först, S. O. Mariager, M. Chollet, H. T. Lemke, J. S. Robinson, J. M. Glownia, M. P. Minitti, A. Frano, M. Fechner, N. A. Spaldin, T. Loew, B. Keimer, A. Georges, and A. Cavalleri, Nature **516**, 71 (2014).

[21] M. Kozina, M. Fechner, P. Marsik, T. van Driel, J. M. Glownia, C. Bernhard, M. Radovic, D. Zhu, S. Bonetti, U. Staub, and M. C. Hoffmann, Nat. Phys. **15**, 387 (2019).

[22] G. Khalsa and N. A. Benedek, Npj Quantum Mater. **3**, 15 (2018).

[23] C. C. Homes, T. Timusk, D. A. Bonn, R. Liang, and W. N. Hardy, Can. J. Phys. **675**, 663 (1995).

[24] http://elk.sourceforge.net, (n.d.).

[25] R. Mankowsky, M. Fechner, M. Först, A. von Hoegen, J. Porras, T. Loew, G. L. Dakovski, M. Seaberg, S. Möller, G. Coslovich, B. Keimer, S. S. Dhesi, and A. Cavalleri, Struct. Dyn. **4**, 044007 (2017).

[26] A. Togo and I. Tanaka, Scr. Mater. **108**, 1 (2015).